Asymmetrical electro-hydrogenation of CO2 to ethanol with Copper-Gold heterojunctions

PNAS RESEARCH ARTICLE | CHEMISTRY

Asymmetrical electrohydrogenation of CO_2 to ethanol with copper–gold heterojunctions

Siyu Kuang[a], Yaqiong Su[b], Minglu Li[a], Hai Liu[a], Hongyuan Chuai[a], Xiaoyi Chen[a], Emiel J. M. Hensen[c], Thomas J. Meyer[d,1], Sheng Zhang[a,1], and Xinbin Ma[a,1]

Contributed by Thomas J. Meyer; received August 18, 2022; accepted December 18, 2022; reviewed by Héctor D. Abruña and Andrew B. Bocarsly

Copper is distinctive in electrocatalyzing reduction of CO_2 into various energy-dense forms, but it often suffers from limited product selectivity including ethanol in competition with ethylene. Here, we describe systematically designed, bimetallic electrocatalysts based on copper/gold heterojunctions with a faradaic efficiency toward ethanol of 60% at currents in excess of 500 mA cm^{-2}. In the modified catalyst, the ratio of ethanol to ethylene is enhanced by a factor of 200 compared to copper catalysts. Analysis by ATR-IR measurements under operating conditions, and by computational simulations, suggests that reduction of CO_2 at the copper/gold heterojunction is dominated by generation of the intermediate OCCOH*. The latter is a key contributor in the overall, asymmetrical electrohydrogenation of CO_2 giving ethanol rather than ethylene.

copper | ethanol | heterojunction | CO_2 | hydrogenation

Significance

Electrochemical CO_2 reduction is a promising strategy to store renewable electrical energy in the chemical bonds of carbon fuels. Currently, high performance has been reported for C_1 products, like CO and formate, which are selectively produced by a number of catalysts through $2e^-/2H^+$ steps. Due to shared reaction pathways, ethanol is always produced competitively with ethylene. A copper/gold heterojunction catalyst is reported here for the selective production of ethanol through asymmetrical electrohydrogenation of CO_2. It is shown that bimetallic Cu/Au exhibits a 200-fold enhancement in the ratio of ethanol to ethylene compared with a single Cu catalyst.

An important approach to global warming, and the energy crisis (1), is based on electrochemical reduction of CO_2 with solar, wind, or other renewable energies (2–4). Of the reduction products, the C_{2+} chemicals, ethylene and ethanol, have high energy densities with significant global market values (5–7). High faradaic efficiencies and current densities have already been achieved for CO_2 reduction to $2e^-$ products, like CO and formate based on a number of catalysts (8–11). However, copper-based catalysts provide significant examples of metallic catalysts that generate C_{2+} products (12–14). There are complications in this chemistry from shared reaction pathways. Key intermediates are produced that can lead to ethylene or ethanol competitively (13, 15). Enhanced ethylene production has been achieved by implementing Cu-based catalysts via materials engineering (16–18). Efficient ethanol production by CO_2 reduction still remains a major challenge (19–21).

Recently, new strategies have appeared for improving CO_2 reduction to ethanol. Ren et al. used an oxide-derived Cu_xZn catalyst that enhanced CO_2 electroreduction to ethanol. A two-site mechanism was proposed in which CO, generated at zinc sites, transferred to neighboring copper sites where C–C coupling occurs to form ethanol (15). Similarly, Morales-Guio et al. investigated the synergistic effect of a bimetallic Au/Cu catalyst for promoting ethanol formation (22). In a related study, Ag was also introduced to manipulate Cu surfaces. Addition of Ag enhances the diversity of binding sites which disrupts the coordination environment for intermediates on pathways for ethylene formation (19). However, ethanol selectivity in these studies was < 30%, far lower than industrial requirements.

A recent approach, with high ethanol selectivity, was reported by Xu et al. (23). It was based on an atomically dispersed copper catalyst, but its low current density, 1.23 mA cm^{-2}, was well below that needed for industrial requirements of > 200 mA cm^{-2}. In accelerating the rate in aqueous solutions, a gas-phase CO_2 supply could help to overcome slow CO_2 diffusion (24). New approaches are required to improve both ethanol selectivity and current density (25, 26).

The approach taken here was to focus on bimetallic Cu–Au catalysts with the utilization of density functional theory (DFT) to examine possible reaction pathways with an electrostatic self-assembly strategy to fabricate Cu/Au heterojunctions. Comparing single Au, single Cu, CuAu alloys, and isolated Cu–Au mixtures reveals that only Cu/Au heterojunctions display a high faradaic efficiency for ethanol (~60%). With a gas diffusion electrode, current densities as high as ~500 mA cm^{-2} were observed that exceed values for practical CO_2 electrolysis. In ethanol synthesis, in situ ATR-IR analysis has detected the key intermediate, OCCOH*, consistent with the results of DFT calculations.

Results

Previous reports have shown that ethylene is the main C_2 product on Cu. CO is the main product on a CuAu alloy (27, 28). There are also trace amounts of ethanol with the bimetallic CuAu catalyst (22). In the current study, Cu/Au heterojunctions are compared with Cu and CuAu alloy for reactivity comparisons.

Author contributions: S.Z. designed research; S.K., Y.S., and M.L. performed research; Y.S. and E.J.M.H. contributed new reagents/analytic tools; S.K., H.L., H.C., X.C., T.J.M., S.Z., and X.M. analyzed data; and S.K., T.J.M., S.Z., and X.M. wrote the paper.

Reviewers: H.D.A., Cornell University; and A.B.B., Princeton University.

The authors declare no competing interest.

[1]To whom correspondence may be addressed. Email: tjmeyer@unc.edu, sheng.zhang@tju.edu.cn, or xbma@tju.edu.cn.

This article contains supporting information online at https://www.pnas.org/lookup/suppl/doi:10.1073/pnas.2214175120/-/DCSupplemental.

Published January 17, 2023.

Reaction pathways that lead to key products from CO_2 on CuAu, Cu/Au, and Cu as catalysts are shown in Fig. 1*A* and *SI Appendix*, Figs. S1 and S2. From the data, CO is a key intermediate in the preparation of nonformate products. On the surface of CuAu, CO* binding is relatively weak, while CO* adsorption on both Cu and Cu/Au is more highly favored.

Reaction pathways involving formation of OCCO* and HCO* from CO are shown in Fig. 1*B*. The data for Cu and CuAu show that the appearance HCO* as an intermediate is in competition with OCCO* with the relative energies of 1.79 and 1.38 eV. At Cu/Au heterojunctions, direct CO coupling is favored ($\Delta G = 0.52$ eV). C_2H_4 is more easily prepared at Cu by 2HCO* coupling through the intermediate CHOCHO*. The interface, Cu/Au, appears to give C_2H_5OH by asymmetric hydrogenation of OCCO* through the intermediate OCCOH*.

Free energy profiles for the reduction of CO_2 to ethylene and ethanol over Cu/Au and Cu are shown in Fig. 1 *C* and *D*. As shown in Fig. 1*C*, a reaction pathway, that includes as an intermediate OCCOH* for C_2H_5OH production at Cu/Au heterojunctions, occurs in the occurs in the sequence: $CO_2 \rightarrow CO_2^* \rightarrow CO^* \rightarrow 2CO^* \rightarrow OCCO^* \rightarrow$ OCC OH* $\rightarrow$ OC C* $\rightarrow$ OCC H* $\rightarrow$ OCC H_2* $\rightarrow$ OCC H_3* $\rightarrow$ $OCHCH_3^* \rightarrow HOCHCH_3^* \rightarrow HOCH_2CH_3^* \rightarrow C_2H_5OH$.

The pathway leading to the appearance of C_2H_4 on Cu has different properties. In ethylene formation, a key intermediate is CHOCHO* rather than OCCOH*. Once formed, the latter is followed by sequential, symmetric hydrogenation to give C_2H_4 through the reaction sequence: $CO_2 \rightarrow CO_2^* \rightarrow CO^* \rightarrow 2CO^* \rightarrow 2HCO^* \rightarrow CHOCHO^* \rightarrow CHOCHOH^* \rightarrow CHOHCHOH^* \rightarrow CHCHOH^* \rightarrow CH_2CHOH^* \rightarrow C_2H_4 + H_2O$ (Fig. 1*D*).

Reactivity at Cu/Au interfaces is shown in Fig. 1*E*. At the surface, selective formation of C_2H_5OH at Cu/Au originates based on the asymmetrical adsorption geometry of OCCO*. In the intermediate, one carbon atom is bound to Au and the second to Cu with enhanced adsorption energy on Cu. The combined interaction between sites leads to preferential hydrogenation of OCCO* at the carbon atom once it is bound to Cu to give the intermediate OCCOH*.

In the overall reaction pathway, asymmetrical electrohydrogenation leads to an $OCCH_3$ intermediate. The latter dictates the major product, ethanol. In the scheme, the Cu/Au heterojunctions play a major role in ethanol generation during the reduction of CO_2.

Cu/Au heterojunctions were fabricated through well-designed electrostatic self-assembly of positively charged copper and negatively charged gold nanoparticles, as shown in Fig. 2*A* (29, 30). High-resolution, transmission electron microscopic (HRTEM) images (*SI Appendix*, Fig. S3) of Cu/Au electrodes provide evidence for definite crystalline planes with an interplanar spacing of 2.32 Å and 2.39 Å. The latter correspond to the facets of CuO (111) and Au (111). Analysis of the aberration-corrected transmission electron microscopic images led to characterization of the interfacial structure between Cu and Au particles.

As shown in Fig. 2*B*, the atomic arrangements of Cu and Au particles cross each other at the interface and the further EDX analysis shows a clear interfacial connection between copper and gold (*SI Appendix*, Fig. S4), consistent with formation of Cu/Au heterojunctions during the synthesis of a tandem Cu/Au interface. TEM images in Fig. 2 *C*–*F* show that the synthesis of control

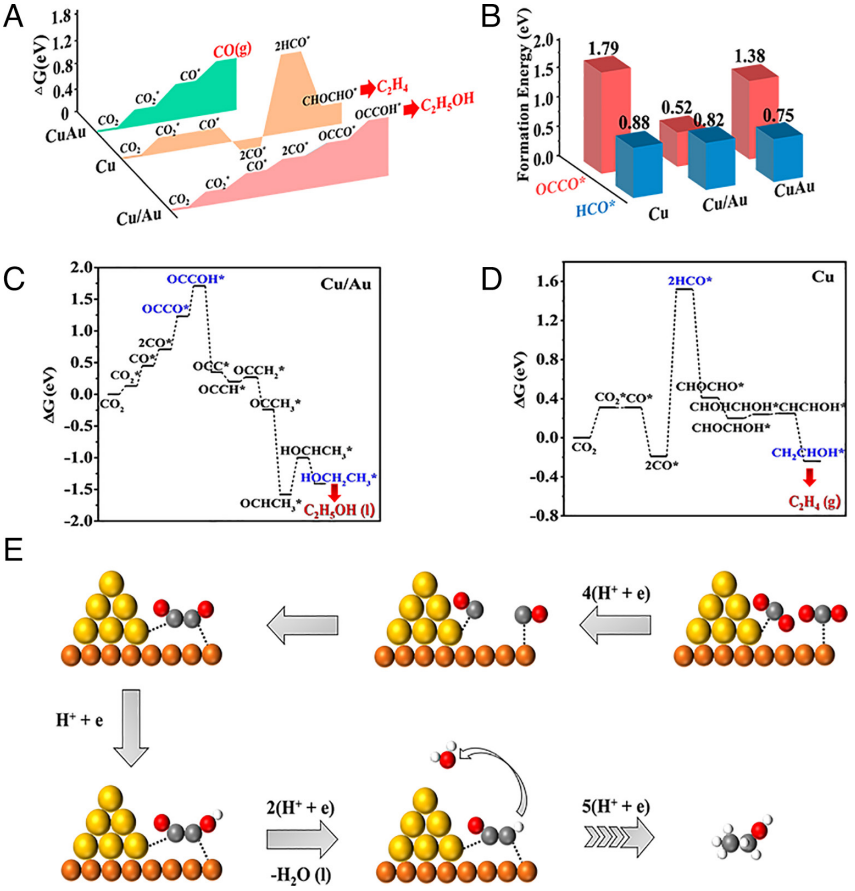

Fig. 1. (*A*) Energy diagrams for CO_2 reduction on CuAu, Cu/Au, and Cu. (*B*) Histograms showing formation energies (eV) for OCCO* and HCO* on CuAu, Cu/Au, and Cu. Free energy diagram for the electrochemical reduction of CO_2 on (*C*) Cu/Au and (*D*) Cu. (*E*) An energy diagram for generating C_2H_5OH from CO_2 that features proton-coupled electron transfer on Cu/Au with Cu, brown; Au, yellow; C, gray; O, red; and H, white.

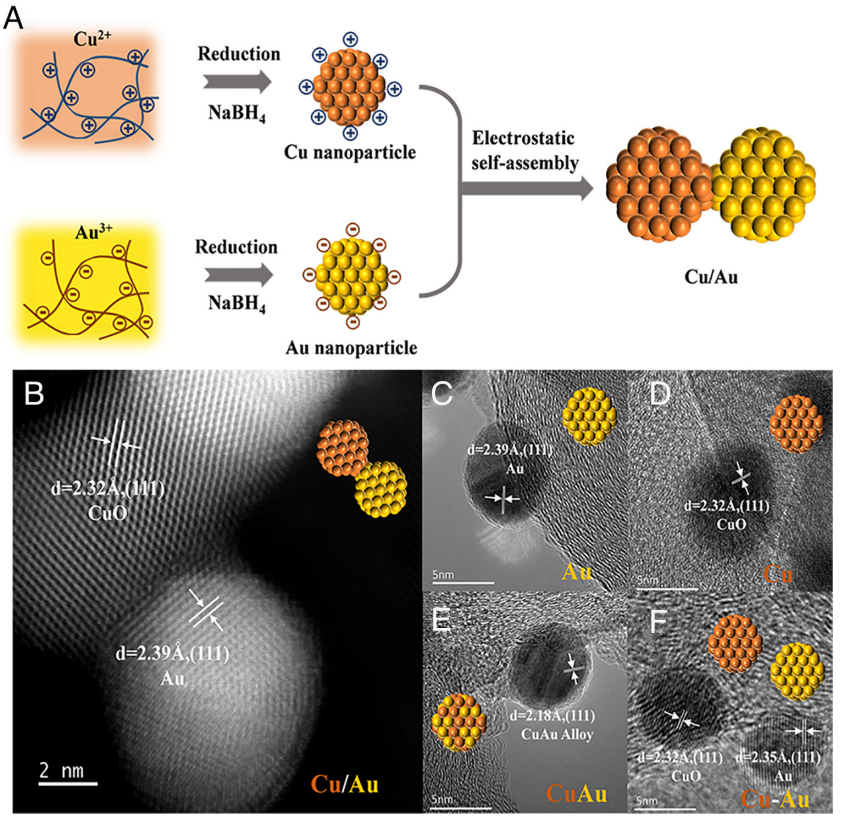

Fig. 2. (*A*) Schematic illustration of the fabrication of Cu/Au nanoparticle. (*B*) Aberration-corrected TEM images of Cu/Au heterojunctions with an illustrative, schematic diagram showing a structural schematic diagram in the *Inset*. HRTEM images and structural schematic diagrams (*Inset*) for (*C*) Au nanoparticles, (*D*) Cu nanoparticles, (*E*) CuAu alloy, and (*F*) isolated Cu–Au particles.

samples including Au, Cu, and CuAu alloys and isolated Cu–Au composites, all loaded on carbon substrates.

X-ray diffraction patterns are shown in *SI Appendix*, Fig. S3. For the Cu/Au sample, three well-defined diffraction peaks at 2θ ≈ 35.5°, 38.7°, and 48.7° were attributable to the (11-1), (111), and (20-2) planes of CuO (PDF: 48-1548), respectively. Diffraction peaks at 2θ ≈ 38.1°, 44.4°, 64.6°, 77.5°, and 81.7° were assignable to the (111), (200), (220), (311), and (222) planes of Au (PDF: 04-0874), respectively. Analysis of the data was consistent with Cu/Au heterojunctions that consist of Cu and Au phases.

Electrocatalytic carbon dioxide reduction was investigated in a H cell under CO_2-saturated, 0.1 M $KHCO_3$ aqueous solutions. As shown in *SI Appendix*, Fig. S5, CO was identified as a major product on Au and CuAu alloys and isolated Cu–Au mixtures, and C_2H_4 as the main C_2 product on Cu catalytic surfaces. Ethanol was the main C_2 product on Cu/Au heterojunctions with a maximum ethanol Faradaic efficiency reached at −0.8 V. Only trace amounts of ethanol were detected on Cu and separation Au–Cu samples. Notably, the Faradaic efficiency ratio of ethanol over ethylene on Cu/Au heterojunctions was significantly enhanced by a factor of 200 compared with Cu at −0.8 V (83 vs. 0.41), as shown in Fig. 3*A*. The latter is consistent with ethanol formation largely promoted on Cu/Au heterojunctions.

In previous studies, it was claimed that in tandem Au/Cu catalysis, Au nanoparticles reduce CO_2 to CO with the latter migrating to neighboring Cu surfaces for C–C coupling (22). As shown in *SI Appendix*, Fig. S4*B*, with CO as the feed gas, ethanol production on Cu was increased relative to CO_2, but the Faradaic efficiency for ethanol was still low (~10%). The decrease points to CO, not necessarily a key contributor to high ethanol selectivity.

The optimal catalyst loading on carbon substrates was found to be 40% giving an ethanol Faradaic efficiency of 43% shown in *SI Appendix*, Figs. S6 and S7. The impact of the Cu/Au catalyst was further evaluated by varying the Au to Cu ratio. Decreasing the ratio of Cu to Au leads to an increase in ethanol Faradaic efficiency that reaches 50% at a ratio of 1/2 (*SI Appendix*, Fig. S7). Based on the results of high-resolution X-ray photoelectron spectroscopic analysis (*SI Appendix*, Fig. S8), the more intense Cu^+/Cu^0 peak that appears in the spectrum, with a decrease in lattice oxygen, shows that oxygen vacancies are generated on the partially reduced sample (31). As shown in Fig. 3*B*, the Faradaic efficiency for ethanol was improved to 60% at −0.8 V for partially reduced Cu/Au heterojunctions.

In CO_2 reduction at gas diffusion electrodes (GDE), the gaseous CO_2 feed helps to overcome slow CO_2 transport. The latter is inherent in H cells and limits reaction rates (32). To demonstrate the behavior of the Cu/Au heterojunctions under industrial conditions, we evaluated CO_2 reduction in a flow cell coupled with a gas diffusion electrode (*SI Appendix*, Fig. S9). Gas-diffusion electrodes, that use gaseous reactants such as oxygen or carbon dioxide, can be used with vapor-fed injection in electrolytically wetted porous structures. Alterations in local reaction microenvironments can result in enhanced hydroxide activities at the electrode surface where water activity is lower. In proton-consuming CO_2 reduction, variations in pH can also lead to variations in reaction products.

Our investigation of CO_2 reduction utilized a GDE with a high ethanol Faradaic efficiency of 60% in 1 M KOH at −0.75 V, where liquid products were determined by NMR spectra shown in *SI Appendix*, Fig. S10. *SI Appendix*, Figs. S11 and S12 summarize Faradaic efficiencies (%) for all reduction products from CO_2 reduction for flow cell tests in 1 M KOH and 0.1 M $KHCO_3$, respectively. Equal maximum Faradaic efficiencies of ethanol (~60%) were

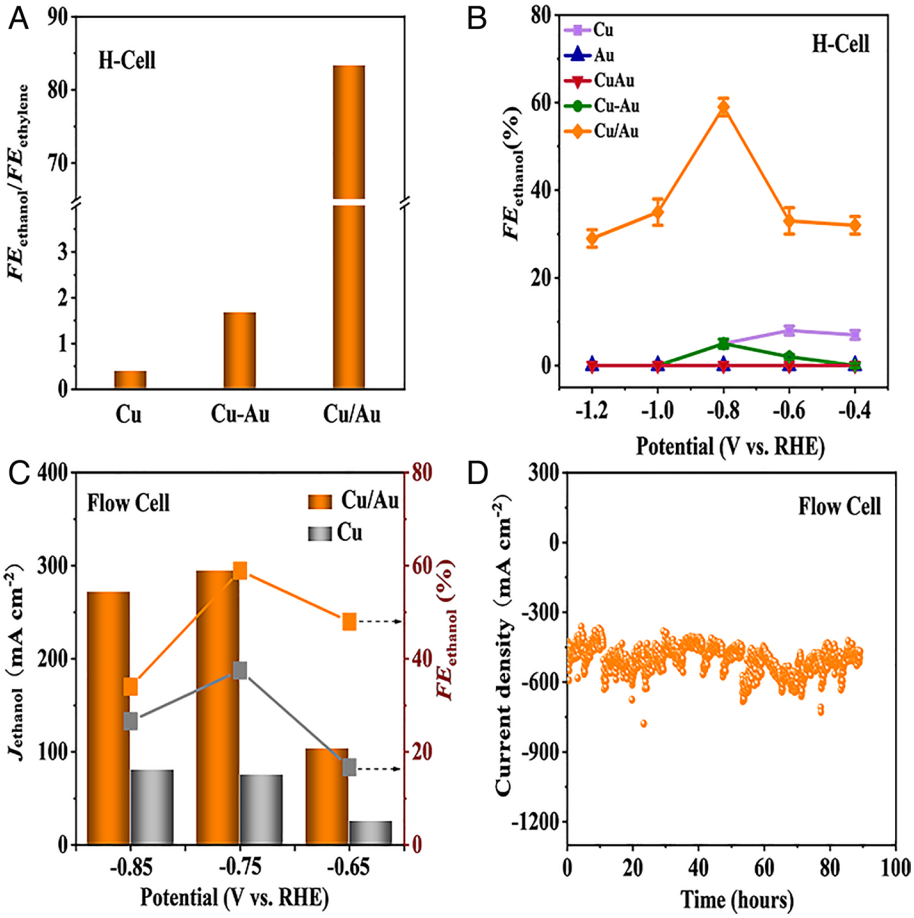

Fig. 3. CO_2RR performances in H cells: (*A*) Ratios of Faradaic efficiency ratios for ethanol to ethylene on Cu, Cu–Au, and Cu/Au in 0.1 M CO_2-saturated $KHCO_3$ aqueous solutions at −0.8V vs. RHE. (*B*) Faradaic efficiencies (%) for the appearance of ethanol at Cu, Au, CuAu, Cu–Au, and Cu/Au in 0.1 M CO_2-saturated $KHCO_3$ aqueous solutions as a function of applied potential. CO_2RR performances in flow cell: (*C*) Partial current densities for producing ethanol at Cu/Au heterojunctions and Cu particles in 1 M KOH electrolyte at various *IR*-corrected potentials. (*D*) Long-term electrode stability test of the GDE with the best Cu/Au catalysts (at a ratio of 1/2) in 1 M KOH electrolyte at a constant applied potential of −0.75 V vs. RHE.

observed in both electrolytes due to similar local chemical environments (including CO_2 and bicarbonate) created on electrode surface during CO_2RR operation. Partial current densities for ethanol formation, as a function of applied potential, are shown in Fig. 3*C*. The ethanol partial current density of ~300 mA cm^{-2} on Cu/Au, at −0.75V vs. RHE, is a factor of 4 higher than at Cu. Fig. 3*D* shows a long term of electrode stability for over 90 h with an average current density of ~500 mA cm^{-2} at −0.75 V. *SI Appendix*, Fig. S13 summarizes the state-of-the-art in CO_2 reduction in the production of ethylene, ethanol, carbon monoxide, and formate. As shown in *SI Appendix*, Table S1, our Cu/Au heterojunctions output the highest ethanol partial current density among the reported catalysts. We further calculated carbon mass balance in flow cells in 1 M KOH (*SI Appendix*, Fig. S14) and found that 7.5% of carbon was converted to CO_2RR products, which is close to the values (~7.6%) reported in the literature (33). In addition, the cathode energy efficiency was calculated to be 39.8% at an applied potential of −1 V vs. RHE (without considering any IR compensation).

Discussion

Evaluation of the ethanol formation mechanism at Cu/Au heterojunctions utilized potential-dependent, ATR-IR measurements (*SI Appendix*, Fig. S15) showing evidence for the key intermediate OCCOH* as predicted by the DFT calculations. Fig. 4*A* shows potential-dependent, absorption spectra for Cu/Au in CO_2-saturated 0.1 M $KHCO_3$ with bands appearing from 2,250-1,000 cm^{-1}. The corresponding spectra for Au and Cu were given in *SI Appendix*, Figs. S16 and S17, respectively. A band at 1,640 cm^{-1} appears arising from a O–H bending mode for H_2O (34). A reversible band at 1,225 cm^{-1} appears from an O–Si–O stretching vibration in the SiO_2 overlayer on a silicon prism substrate.

Increasing the potential of the electrode negatively past −0.8 V led to the accelerated appearance of gaseous products. Under these conditions, the catalyst layer was detached from the Si surface. Surface measurements showed that loss of the catalyst layer was accompanied by the appearance of surface O–Si–O vibrations (35). A band at 2,110 cm^{-1} was assignable to a line-bound CO (CO_L). The latter shifts to lower energies at negative scans (*SI Appendix*, Fig. S18), consistent with the appearance of a Stark effect, as described in earlier reports.

As shown in Fig. 4*A*, the bands at 1,640 and 1,109 cm^{-1} are sensitive to changes in scan rates. They appear at negative potentials and require CO_2 for their appearance during CO_2 reduction. As predicted earlier, they may be attributed to OCCOH*. As shown in the DFT calculations in *SI Appendix*, Fig. S19, in the spectrum of OCCOH*, a C=O stretch appears at 1,593 cm^{-1} and a C–OH band at 1,117 cm^{-1}. The C–OH band is consistent with the experimental result at 1,109 cm^{-1}, and the C=O band with the experimental result at 1,640 cm^{-1}.

Hydroxypropanone with a carbonyl group adjacent to hydroxyl (OCCOH) was selected as a surrogate to further prove the assignment of the bands cited above to the key intermediate OCCOH*. As shown in Fig. 4*B*, a band at ~1,099 cm^{-1} detected on Cu/Au heterojunction

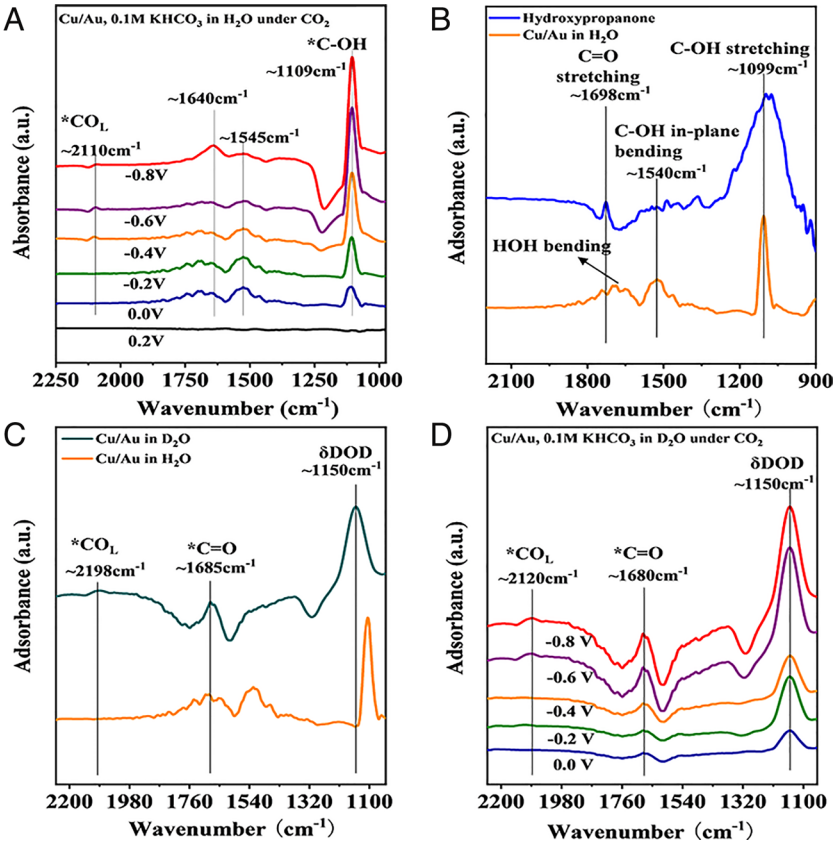

Fig. 4. Potential-dependent, attenuated total reflection infrared (ATR-IR) spectra on Cu/Au heterojunctions. (*A*) Full-range spectra on Cu/Au heterojunctions in CO_2-saturated 0.1M $KHCO_3$ from 0.2V vs. RHE to −0.8V vs. RHE. (*B*) Full-range spectra on Cu/Au heterojunctions in CO_2-saturated 0.1M $KHCO_3$ (orange) and hydroxypropanone (blue) at −0.4V vs. RHE. (*C*) Full-range spectra on Cu/Au heterojunctions with H_2O as electrolyte (orange) and with D_2O as electrolyte (dark green) in CO_2-saturated 0.1M $KHCO_3$ at −0.4V vs. RHE. (*D*) Full-range spectra on Cu/Au heterojunctions with D_2O as electrolyte in CO_2-saturated 0.1M $KHCO_3$ from 0V vs. RHE to −0.8V vs. RHE.

during CO_2RR at −0.4V is consistent with the C–OH stretch of hydroxypropanone. Unfortunately, water exhibits a wide O–H bending band in the 1,700-1,550 cm^{-1} range, which may overlay the signal of C=O vibration. To prove the point, CO_2RR on a Cu/Au heterojunction was performed in heavy water D_2O where O-D bending peak shifts to around 1,150 cm^{-1}. In D_2O solution shown in Fig. 4*C*, a band around 1,685 cm^{-1} was still observed, which is consistent with C=O stretching of hydroxypropanone. This suggests that in Fig. 4*A*, the peak at 1,640 cm^{-1} indeed originates from the C=O stretch. Moreover, in Fig. 4*D*, the C=O stretch at ~1,680 cm^{-1} in D_2O solution, increases under more negative potentials, and shows the same trend with the C–OH band at ~1,109 cm^{-1} (increasing with more negative potentials in H_2O electrolyte) as shown in Fig. 4*A*. These results clearly indicate the formation of the intermediate OCCOH* during CO_2 reduction over Cu/Au heterojunctions, while the intermediate was not detected over single Cu and single Au samples.

Based on the DFT analysis, the intermediate OCCOH* adsorbs at Cu/Au heterojunctions with a single carbon atom bound to Au and the other to Cu. The high hydrogenation activity at Cu is caused by the carbon atom bound to Cu (C=O). The latter forms C–OH which undergoes hydrogenation at more negative potentials consistent with a strong interaction between C–OH and Cu. By contrast, the C=O interaction with Au tends to lead to desorption at more negative potentials (~−0.8 V).

Conclusion

We have described an optimized procedure for the electrocatalytic reduction of CO_2 to ethanol based on the rational design and modification of bimetallic catalysts. Electrocatalytic results show that Cu/Au heterojunctions can lead to the selective conversion of CO_2 to ethanol in 60% yield, a result in agreement with the results of DFT calculations. Exploitation of the reactivity toward CO_2 was extended by using a GDE, resulting in a long-term electrode stability of over 90 h at 500 mA cm^{-2}.

Utilization of in situ ATR-IR spectroscopy reinforces the results of computational calculations with both pointing to the appearance of the intermediate OCCOH* as an important element in the asymmetrical electrohydrogenation of CO_2 to ethanol. The overall results presented here also highlight the fact that utilization of Cu/Au heterojunctions can occur under conditions appropriate for the formation of ethanol under conditions appropriate for industrial production.

Materials and Methods

Full experimental details and procedures for the synthesis of the samples used in the present study are described in *SI Appendix*.

Data, Materials, and Software Availability. All study data are included in the article and/or *SI Appendix*.

ACKNOWLEDGMENTS. We are grateful to the financial support from the National Nature Science Foundation of China (Grant nos. 22078232 and 21938008) and the Science and Technology Major Project of Tianjin (Grant nos. 19ZXNCGX00030 and 20JCYBJC00870). Y. S. acknowledges the "Young Talent Support Plan" of Xi'an Jiaotong University. Supercomputing facilities were provided by Hefei Advanced Computing Center.

Author affiliations: [a]Key Laboratory for Green Chemical Technology of Ministry of Education, School of Chemical Engineering and Technology, Tianjin University, Tianjin 300072, China; [b]School of Chemistry, Xi'an Key Laboratory of Sustainable Energy Materials Chemistry, State Key Laboratory of Electrical Insulation and Power Equipment, Xi'an Jiaotong University, Xi'an 710049, China; [c]Department of Chemical Engineering and Chemistry, Laboratory of Inorganic Materials and Catalysis, Eindhoven University of Technology, 5600 MB, Eindhoven, The Netherlands; and [d]Department of Chemistry, University of North Carolina at Chapel Hill, Chapel Hill, NC 27599

1. J. D. Shakun *et al.*, Global warming preceded by increasing carbon dioxide concentrations during the last deglaciation. *Nature* **484**, 49–54 (2012).
2. D. U. Nielsen, X.-M. Hu, K. Daasbjerg, T. Skrydstrup, Chemically and electrochemically catalysed conversion of CO_2 to CO with follow-up utilization to value-added chemicals. *Nat. Catal.* **1**, 244–254 (2018).
3. Y. Hori, "Electrochemical CO_2 reduction on metal electrodes" in *Modern Aspects of Electrochemistry* (Springer, 2008), **vol. 42**, pp. 89–189.
4. S. Zhang, Q. Fan, R. Xia, T. J. Meyer, CO_2 reduction: From homogeneous to heterogeneous electrocatalysis. *Acc. Chem. Res.* **53**, 255–264 (2020).
5. M. Jouny, W. Luc, F. Jiao, General techno-economic analysis of CO_2 electrolysis systems. *Ind. Eng. Chem. Res.* **57**, 2165–2177 (2018).
6. S. Zhang *et al.*, Polymer-supported CuPd nanoalloy as a synergistic catalyst for electrocatalytic reduction of carbon dioxide to methane. *Proc. Natl. Acad. Sci. U.S.A.* **112**, 15809–15814 (2015).
7. S. Zhang, P. Kang, T. J. Meyer, Nanostructured tin catalysts for selective electrochemical reduction of carbon dioxide to formate. *J. Am. Chem. Soc.* **136**, 1734–1737 (2014).
8. H. Yang, J. J. Kaczur, S. D. Sajjad, R. I. Masel, Electrochemical conversion of CO_2 to formic acid utilizing sustainion membranes. *J. CO2 Util.* **20**, 208–217 (2017).
9. X. Lu *et al.*, High performance electrochemical CO_2 reduction cells based on non-noble metal catalysts. *ACS Energy Lett.* **3**, 2527–2532 (2018).
10. J. J. Kaczur, Y. Hongzhou, L. Zengcai, S. D. Sajjad, R. I. Masel, Carbon dioxide and water electrolysis using new alkaline stable anion membranes. *Front. Chem.* **6**, 263 (2018).
11. D. A. Salvatore, D. M. Weekes, J. He, K. E. Dettelbach, C. P. Berlinguette, Electrolysis of gaseous CO_2 to CO in a flow cell with a bipolar membrane. *ACS Energy Lett.* **3**, 149–154 (2017).
12. Y. Hori, A. Murata, R. Takahashi, Formation of hydrocarbons in the electrochemical reduction of carbon dioxide at a copper electrode in aqueous solution. *J. Chem. Soc. Faraday Trans.* **85**, 2309–2326 (1989).
13. K. P. Kuhl, E. R. Cave, D. N. Abram, T. F. Jaramillo, New insights into the electrochemical reduction of carbon dioxide on metallic copper surfaces. *Energy Environ. Sci. Technol.* **5**, 7050–7059 (2012).
14. S. Kuang *et al.*, Stable surface-anchored Cu nanocubes for CO_2 electroreduction to ethylene. *ACS Appl. Nano Mater.* **3**, 8328–8334 (2020).
15. D. Ren, B.S.-H. Ang, B. S. Yeo, Tuning the selectivity of carbon dioxide electroreduction toward ethanol on oxide-derived CuxZn Catalysts. *ACS Catal.* **6**, 8239–8247 (2016).
16. C. T. Dinh *et al.*, CO_2 electroreduction to ethylene via hydroxide-mediated copper catalysis at an abrupt interface. *Science* **360**, 783–787 (2018).
17. S. Ma *et al.*, One-step electrosynthesis of ethylene and ethanol from CO_2 in an alkaline electrolyzer. *J. Power Source* **301**, 219–228 (2016).
18. T. T. H. Hoang *et al.*, Nano porous copper-silver alloys by additive-controlled electrodeposition for the selective electroreduction of CO_2 to ethylene and ethanol. *J. Am. Chem. Soc.* **140**, 5791–5797 (2018).
19. Y. C. Li *et al.*, Binding site diversity promotes CO_2 electroreduction to ethanol. *J. Am. Chem. Soc.* **141**, 8584–8591 (2019).
20. Y. Song *et al.*, High-selectivity electrochemical conversion of CO_2 to ethanol using a copper nanoparticle/N-doped graphene electrode. *ChemistrySelect* **1**, 6055–6061 (2016).
21. T. T. Hoang *et al.*, Nanoporous copper–silver alloys by additive-controlled electrodeposition for the selective electroreduction of CO_2 to ethylene and ethanol. *J. Am. Chem. Soc.* **140**, 5791–5797 (2018).
22. C. G. Morales-Guio *et al.*, Improved CO_2 reduction activity towards C_{2+} alcohols on a tandem gold on copper electrocatalyst. *Nat. Catal.* **1**, 764–771 (2018).
23. H. Xu, D. Rebollar, H. He, L. Chong, T. Xu, Highly selective electrocatalytic CO_2 reduction to ethanol by metallic clusters dynamically formed from atomically dispersed copper. *Nat. Energy* **5**, 623–632 (2020).
24. T. N. Nguyen, C. T. Dinh, Gas diffusion electrode design for electrochemical carbon dioxide reduction. *Chem. Soc. Rev.* **49**, 7488–7504 (2020).
25. P. D. Luna, C. Hahn, D. Higgins, S. A. Jaffer, F. T. Jaramillo, What would it take for renewably powered electrosynthesis to displace petrochemical processes? *Science* **364**, eaav3506 (2019).
26. M. B. Ross *et al.*, Designing materials for electrochemical carbon dioxide recycling. *Nat. Catal.* **2**, 648–658 (2019).
27. D. Kim *et al.*, Electrochemical activation of CO_2 through atomic ordering transformations of AuCu nanoparticles. *J. Am. Chem. Soc.* **139**, 8329–8336 (2017).
28. O. A. Baturina *et al.*, CO_2 electroreduction to hydrocarbons on carbon-supported Cu nanoparticles. *ACS Catal.* **4**, 3682–3695 (2014).
29. A. M. Kalsin *et al.*, Electrostatic self-assembly of binary nanoparticle crystals with a diamond-like lattice. *Science* **312**, 420–424 (2006).
30. S. Zhang, Y. Shao, G. Yin, Y. Lin, Electrostatic self-assembly of a Pt-around-Au nanocomposite with high activity towards formic acid oxidation. *Angew. Chem. Int. Ed.* **49**, 2211–2214 (2010).
31. Z. Gu *et al.*, Oxygen vacancy tuning toward efficient electrocatalytic CO_2 reduction to C_2H_4. *Small Methods* **3**, 1800449 (2019).
32. D. M. Weekes, D. A. Salvatore, A. Reyes, A. Huang, C. P. Berlinguette, Electrolytic CO_2 reduction in a flow cell. *Acc. Chem. Res.* **51**, 910–918 (2018).
33. E. W. Lees, B. A. Mowbray, F. G. Parlane, C. P. Berlinguette, Gas diffusion electrodes and membranes for CO_2 reduction electrolysers. *Nat. Rev. Mater.* **7**, 55–64 (2022).
34. J. E. Pander, M. F. Baruch, A. B. Bocarsly, Probing the mechanism of aqueous CO_2 reduction on post-transition-metal electrodes using ATR-IR spectroelectrochemistry. *ACS Catal.* **6**, 7824–7833 (2016).
35. D. Gao *et al.*, Switchable CO2 electroreduction via engineering active phases of Pd nanoparticles. *Nano Res.* **10**, 2181–2191 (2017).